Supporting Information:

Realizing N-type SnTe Thermoelectrics with Competitive Performance through Suppressing Sn Vacancies

Huimei Pang[1], Yuting Qiu[2], Dongyang Wang[1], Yongxin Qin[1], Rong Huang[3], Zhenzhong Yang[3], Xiao Zhang[*,1], Li-Dong Zhao[*,1]

[1]*School of Materials Science and Engineering, Beihang University, Beijing 100191, China*

[2]*Beihang School, Beihang University, Beijing 100191, China*

[3]*Key Laboratory of Polar Materials and Devices (MOE) and Department of Electronics, East China Normal University, Shanghai 200062, China*

E-mail: zhang_xiao@buaa.edu.cn; zhaolidong@buaa.edu.cn

EXPERIMENTAL

Synthesis:

High-purity elements Sn (99.999%), Pb (99.999%), Te (99.999%), SnI_2 (99.999%) were weighed according to the nominal compositions of $Sn_{1-x}Pb_xTe_{0.98}I_{0.02}$ (x = 0.2, 0.3, 0.35, 0.375, 0.4, 0.425, 0.45) and $Sn_{0.6}Pb_{0.4}Te_{1-y}I_y$ (y = 0, 0.010, 0.015, 0.020, 0.025), and then loaded into the 13-mm-diameter fused quartz tubes, flame-sealed at a residual pressure of ~ 10^{-4} Torr. The cubes were first slowly heated from room temperature to 723 K in 12 h, then rapidly heated up to 1423 K in 6 h, maintained at this temperature for 12 h, and cooled to room temperature in the furnace. The obtained ingots were crushed into fine powders and poured into 15 mm diameter graphite dies. Then these powders were densified by spark plasma sintering (SPS) method (SPS-211LX, Fuji Electronic Industrial Co., Ltd.) at 823 K under an axial compressive stress of 40 MPa for 5 min in vacuum. Highly dense (>95% of theoretical density, **Table S1**) disk-shaped pellets of samples were obtained.

Structural characterization:

The phase compositions of all samples were analyzed by X-ray diffraction (XRD), conducted with a D/max 2200PC diffractometer equipped with Cu K_α (λ = 1.5418 Å) radiation and a position-sensitive detector. The samples for structure characterization were prepared by using FEI Helios G4 UX Dualbeam FIB/SEM. Pt and C were coated on the sample surfaces to protect them from Ga ion damage. The cross-sectional lamella was thinned down to ~ 200 nm thick at an accelerating voltage of 30 kV with a current of 0.43 nA, followed by a fine polish at an accelerating voltage of 5 kV and 2 kV with a low current of ~ 68 pA. Scanning transmission electron microscope (STEM) experiments were conducted on a JEM ARM300F under 300 kV. The convergence angle and collection angle for the STEM high-angle annular dark field (HAADF) imaging were 25 and 70–280 mrad, respectively. To reduce the scanning noise and sample drift during acquisition, atomic-resolution HAADF images were obtained by averaging a series of drift-corrected images. HAADF STEM image

simulations were performed by Dr. Probe.[1] The simulation conditions: accelerating voltage ~300 keV; semi-convergence angle ~ 25 mrad; a detector collection range ~ 70 mrad to 280 mrad.

Elastic properties:

The longitudinal (v_l) and shear (v_s) sound velocities were measured using an ultrasonic instrument (Ultrasonic Pulser/Receiver Model 5058 PR, Olympus, USA). Average sound velocity (v_a), Young's modulus (E), shear modulus (G), Poisson ratio (υ_p), and Grüneisen parameter (γ) were calculated from the sound velocities as follows:[2]

$$v_a = \left[\frac{1}{3}\left(\frac{1}{v_l^3}+\frac{2}{v_s^3}\right)\right]^{-1/3} \tag{S1}$$

$$E = \frac{\rho v_s^2\left(3v_l^2-4v_s^2\right)}{\left(v_l^2-v_s^2\right)} \tag{S2}$$

$$\upsilon_p = \frac{1-2\left(v_s/v_l\right)^2}{2-2\left(v_s/v_l\right)^2} \tag{S3}$$

$$G = \frac{E}{2\left(1+\upsilon_p\right)} \tag{S4}$$

$$\gamma = \frac{3}{2}\left(\frac{1+\upsilon_p}{2-3\upsilon_p}\right) \tag{S5}$$

The phonon mean free path (l) could be evaluated using the following equation:[2]

$$\kappa_{lat} = \frac{1}{3}C_v v_a l \tag{S6}$$

where C_v represents the heat capacity at constant volume, which could be substituted by $C_v = C_p\,\rho$ (C_p is heat capacity at constant pressure and ρ is sample density).

Electrical transport properties:

The obtained SPS processed pellets were cut into bars of dimensions 10 mm × 3 mm × 3 mm and used for simultaneously measuring the Seebeck coefficient and electrical conductivity with a Cryoall CTA instrument under a low-pressure helium

atmosphere from room temperature to 823 K. The samples were coated with a thin layer (0.1-0.2 mm) of boron nitride (BN) to protect the instruments from contamination. The uncertainty in the Seebeck coefficient and electrical conductivity measurements is ~ 3 %. Room temperature Hall coefficients were measured under a reversible magnetic field of 1.5 T by the Van der Pauw method using Lake Shore 8400 instrument, and the uncertainty is estimated to be within 5%.[3]

Thermal transport properties:

The obtained pellets were cut into thin wafer with diameter of 8 mm and thickness of 1-2 mm for thermal diffusivity measurements. The samples were coated with a thin layer of graphite to minimize errors from the emissivity of the material. The thermal conductivity was calculated by $\kappa_{tot} = D \cdot C_p \cdot \rho$,[4] where the thermal diffusivity coefficient (D) was measured using the laser flash diffusivity method in a Netzsch LFA457, and was analyzed using a Cowan model with pulse correction. The specific heat capacity (C_p) was calculated using the Debye model,[5] and the sample density (ρ) was determined by the dimensions and mass of the samples. The electronic thermal conductivity (κ_{ele}) was estimated by $\kappa_{ele} = L\sigma T$, where the Lorenz number was calculated based on a single parabolic band (SPB) model.[6] Then the lattice thermal conductivity (κ_{lat}) could be obtained via the relationship: $\kappa_{lat} = \kappa_{tot} - \kappa_{ele}$. The uncertainty of the thermal conductivity is estimated to be within 10%, considering the uncertainties for D, C_p, and ρ. The combined uncertainty for all measurements involved in the calculation of ZT is within 20%.[7]

Density functional theory (DFT) calculations:

First-principles calculation was performed based on the density functional theory (DFT) as implemented in the Vienna ab initio simulation package (VASP).[8-9] The Perdew-Burke-Ernzerhof (PBE)[10] functional of the generalized gradient approximation (GGA) was adopted to describe the exchange-correlation. The electronic wave function was expanded in plane waves with an energy cutoff of 500 eV. The inner coordination of atoms was fully relaxed until the residual forces less

than 0.001 eV A^{-1}. A 3 × 3 × 3 supercell ($Sn_{27}Te_{27}$) was constructed to model one Pb substitution of Sn atom. Considering the symmetry change and band folding due to the substitution in supercell, the electronic band structures were unfolded to primitive Brillouin zone by using BandUP code.[11-12] The Seebeck coefficient and carrier mobility were simulated based on the single band model[13] and deformation potential theory[14], respectively.

Calculation for the specific heat (C_p) through the Debye model:

Based on the Debye model[5] considering the individual contributions of phonon and the effect of thermal expansion, the total specific heat $C_{p,tot}$ as a function of temperature can be obtained as:

$$C_{p,tot}(T) = C_{p,ph}(T) + C_{p,D}(T) \tag{S7}$$

where $C_{p,ph}$ and $C_{p,D}$ represent the phonon specific heat capacity and the effects of lattice dilation on the specific heat capacity, respectively. The contribution of electrons to the heat capacity, as $C_{p,ele}$, was not taken into account, since the effects of dilation is mostly phononic in origin, as $C_{p,ph}$ is much larger than $C_{p,ele}$.

Due to the Debye assumption and elastic wave approximation, the phonon specific heat capacity $C_{p,ph}$ can be written as:

$$C_{p,ph}\left(T/\theta_D\right) = 9R\left(\frac{T}{\theta_D}\right)^3 \int_0^{\theta_D/T} \frac{x^4 e^x}{\left(e^x - 1\right)^2} dx \tag{S8}$$

where θ_D refers to the Debye model, R = 8.314 J $mol^{-1}K^{-1}$, and $x = \hbar\omega/k_B T$, in which $\hbar$, ω and k_B represent Planck constant, phonon vibration frequency and Boltzmann constant, respectively.

The effects of lattice dilation on the total specific heat capacity $C_{p,D}$ can be obtained from:

$$C_{p,D}(T) = C_{ele,D}(T) + C_{ph,D}(T) = \frac{9BT\alpha^2}{10^6 \rho} \tag{S9}$$

where B is the isothermal bulk modulus, α is the linear coefficient of thermal expansion, and ρ is the sample density (all dependent on temperature).

Calculation for the Lorenz number:

An estimation of L can be made using a single parabolic band (SPB) model with acoustic phonon scattering,[6] resulting in a L with a deviation of less than 10% as compared with a more rigorous single non-parabolic band and multiple bands model calculation. Based on the SPB model, the Lorenz number can be given by formula:

$$L = \left(\frac{k_B}{e}\right)^2 \left(\frac{(r+7/2)F_{r+5/2}(\eta)}{(r+3/2)F_{r+1/2}(\eta)} - \left[\frac{(r+5/2)F_{r+5/2}(\eta)}{(r+3/2)F_{r+1/2}(\eta)}\right]^2 \right) \quad \text{(S10)}$$

where k_B is the Boltzmann constant, e is the electric charge, r is the scattering rate, and η refers to the reduced Fermi energy, which can be derived from the measured Seebeck coefficients with consideration of acoustic phonon dominated scattering (r = -1/2) via the following equation:

$$S = \frac{k_B}{e}\left[\frac{(r+5/2)F_{r+3/2}(\eta)}{(r+3/2)F_{r+1/2}(\eta)} - \eta\right] \quad \text{(S11)}$$

$$F_x(\eta) = \int_0^\infty \frac{\varepsilon^x}{1+\exp(\varepsilon-\eta)} d\varepsilon \quad \text{(S12)}$$

$$\eta = \frac{E_f}{k_B T} \quad \text{(S13)}$$

where $F_x(\eta)$ is Fermi integral and E_f is the Fermi energy.

Theoretical calculation of lattice thermal conductivity:

The theoretical lattice thermal conductivity of a material after introducing point imperfections into the host lattice can be estimated by:[15]

$$\frac{\kappa_{lat}}{\kappa_{lat,p}} = \frac{\tan^{-1}(u)}{u} \quad \text{(S14)}$$

where κ_{lat} and $\kappa_{lat,p}$ are the lattice thermal conductivities of the defected and parent materials, respectively. In this work, $\kappa_{lat,p}$ = 2.89 W m^{-1} K^{-1}, u is defined as:

$$u = \left(\frac{\pi^2 \theta_D \Omega}{h v_a^2} \kappa_{lat,p} \Gamma\right)^{1/2} \quad \text{(S15)}$$

$$\theta_D = \frac{h}{k_B}\left(\frac{3}{4\pi\Omega}\right)^{1/3} v_a \quad \text{(S16)}$$

where θ_D, Ω, h, k_B and v_a, are the Debye temperature, average atom volume, Planck constant, Boltzmann constant and average sound velocity, respectively. The imperfection scattering parameter (Γ), is a weighted sum of the mass fluctuation (Γ_M) and strain field fluctuation (Γ_S), can be written as $\Gamma = \Gamma_M + \varepsilon\Gamma_S$. And ε is a phenomenological adjustable parameter related to the Poisson ratio (υ_p) and Grüneisen parameter (γ), and can be expressed by

$$\varepsilon = \frac{2}{9}\left(\frac{6.4\times\gamma\left(1+\upsilon_p\right)}{\left(1-\upsilon_p\right)}\right)^2 \quad \text{(S17)}$$

where υ_p and γ were obtained from sound velocities via Equation S3 and S5, respectively.

For $Sn_{1-x}Pb_xTe_{1-y}I_y$, Γ is defined as:

$$\Gamma_{Sn_{1-x}Pb_xTe_{1-y}I_y} = \frac{1}{2}\left(\frac{M_{(Sn,Pb)}}{\bar{M}}\right)^2 \Gamma_{(Sn,Pb)} + \frac{1}{2}\left(\frac{M_{(Te,I)}}{\bar{M}}\right)^2 \Gamma_{(Te,I)} \quad \text{(S18)}$$

$$\Gamma_{(Sn,Pb)} = \Gamma_{M(Sn,Pb)} + \varepsilon\Gamma_{S(Sn,Pb)} \quad \text{(S19)}$$

$$\Gamma_{M(Sn,Pb)} = x(1-x)\left(\frac{\Delta M_{(Sn,Pb)}}{M_{(Sn,Pb)}}\right)^2 \quad \text{(S20)}$$

$$\Gamma_{S(Sn,Pb)} = x(1-x)\left(\frac{\Delta r_{(Sn,Pb)}}{r_{(Sn,Pb)}}\right)^2 \quad \text{(S21)}$$

$$\Gamma_{(Te,I)} = \Gamma_{M(Te,I)} + \varepsilon\Gamma_{S(Te,I)} \quad \text{(S22)}$$

$$\Gamma_{M(Te,I)} = y(1-y)\left(\frac{\Delta M_{(Te,I)}}{M_{(Te,I)}}\right)^2 \quad \text{(S23)}$$

$$\Gamma_{S(Te,I)} = y(1-y)\left(\frac{\Delta r_{(Te,I)}}{r_{(Te,I)}}\right)^2 \quad \text{(S24)}$$

where $\bar{M}$ represents the average atom mass. $M_{(Sn,Pb)} = (1 - x)M_{Sn} + xM_{Pb}$, $\Delta M_{(Sn,Pb)} = M_{Sn} - M_{Pb}$, $r_{(Sn,Pb)} = (1 - x)r_{Sn} + xr_{Pb}$, $\Delta r_{(Sn,Pb)} = r_{Sn} - r_{Pb}$, and so as $M_{(Te,I)}$, $\Delta M_{(Te,I)}$, $r_{(Te,I)}$, $\Delta r_{(Te,I)}$.

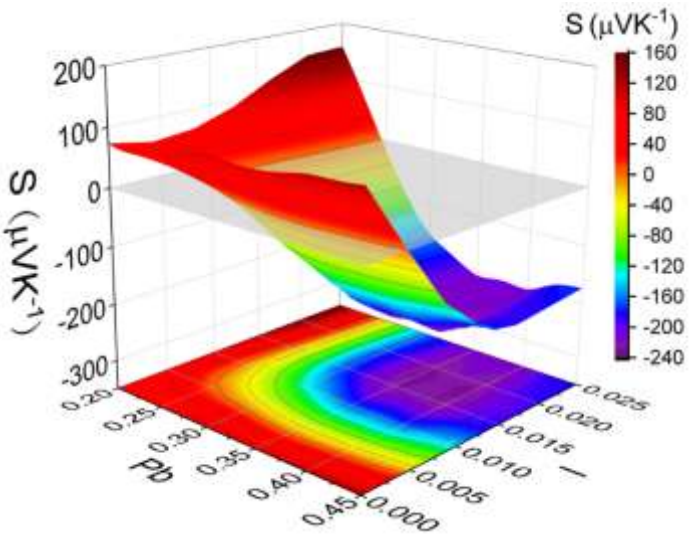

Figure S1. Seebeck coefficient as a function of Pb and I content for $Sn_{1-x}Pb_xTe_{1-y}I_y$ ($0.20 \leq x \leq 0.45, 0 \leq y \leq 0.025$) at 573 K.

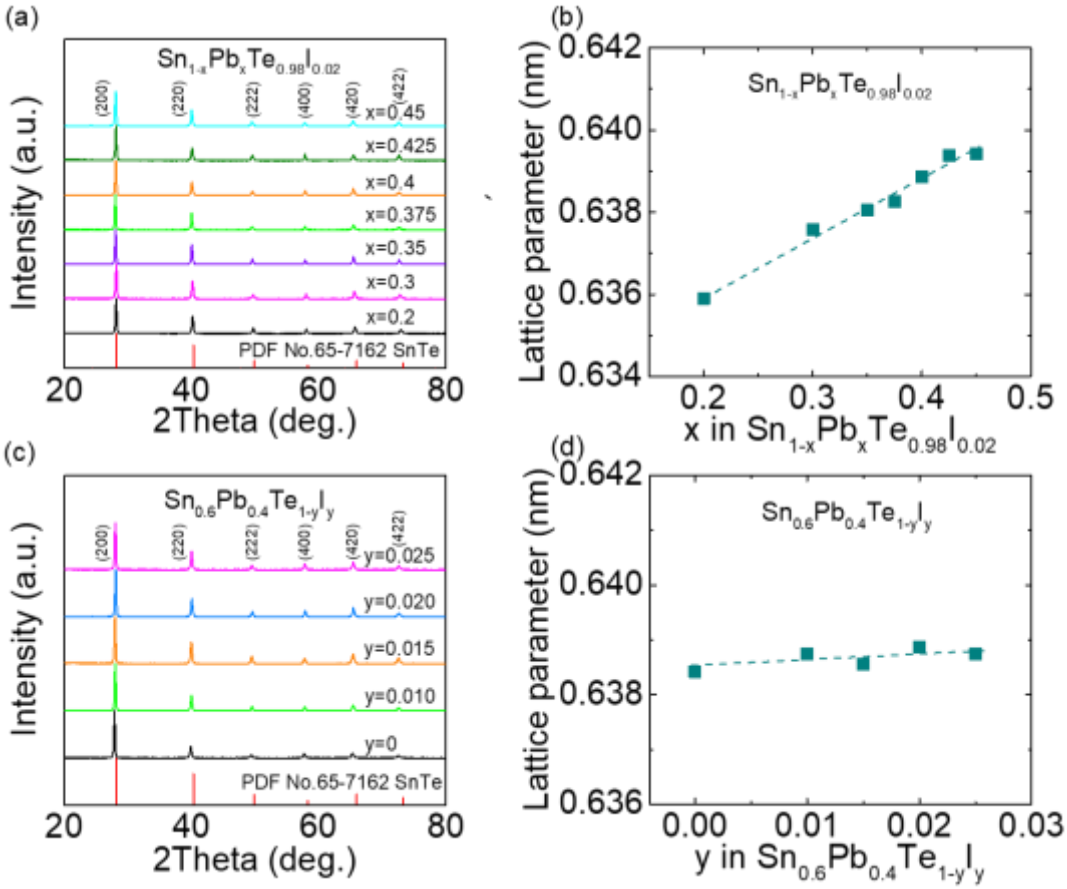

Figure S2. Powder XRD patterns and lattice parameters for (a-b): $Sn_{1-x}Pb_xTe_{0.98}I_{0.02}$ (x = 0.2-0.45), and (c-d): $Sn_{0.6}Pb_{0.4}Te_{1-y}I_y$ (y = 0-0.025).

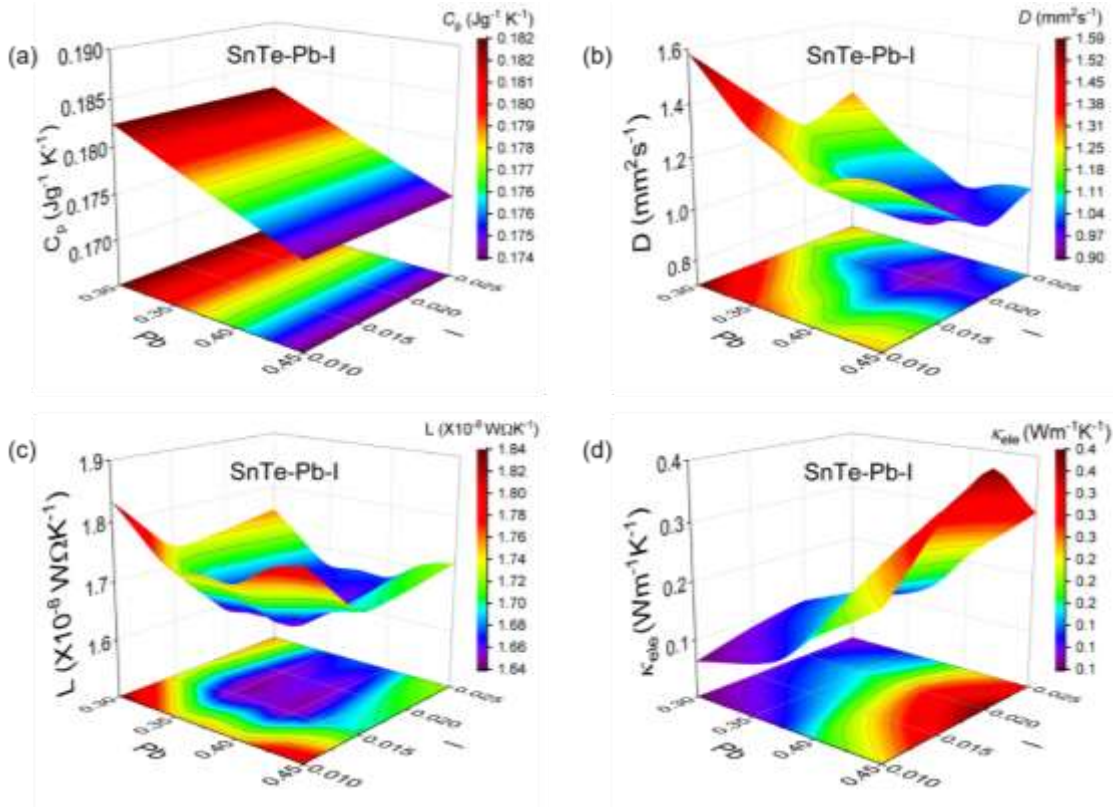

Figure S3. Thermoelectric transport properties as a function of Pb and I content for $Sn_{1-x}Pb_xTe_{1-y}I_y$ ($0.30 \leq x \leq 0.45$, $0.01 \leq y \leq 0.025$) at 573 K: (a) heat capacity; (b) thermal diffusivity; (c) Lorenz number; (d) electronic thermal conductivity.

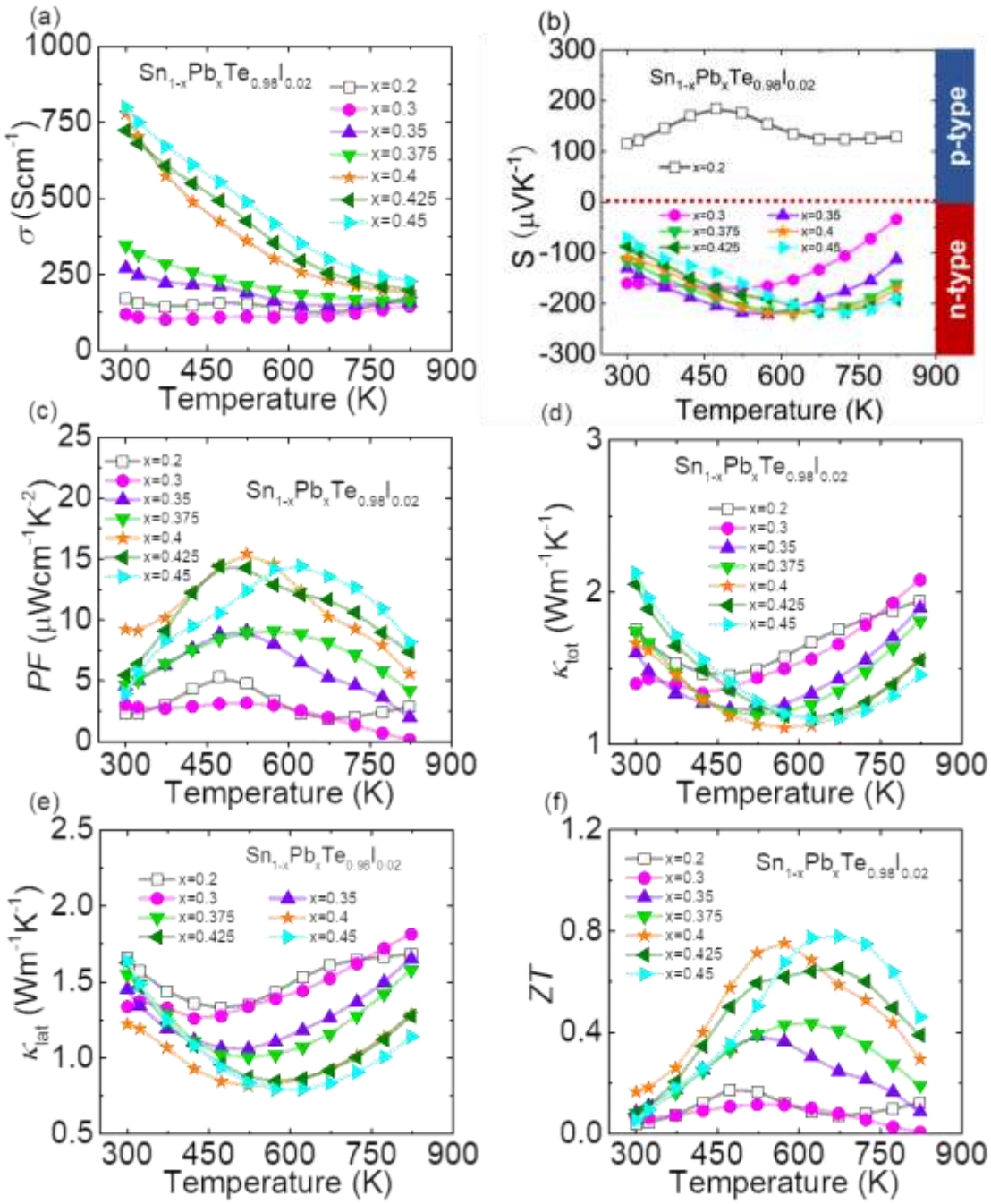

Figure S4. Thermoelectric transport properties as a function of temperature for $Sn_{1-x}Pb_xTe_{0.98}I_{0.02}$ (x = 0.2-0.45): (a) electrical conductivity; (b) Seebeck coefficient; (c) power factor; (d) total thermal conductivity; (e) lattice thermal conductivity; (f) *ZT* value.

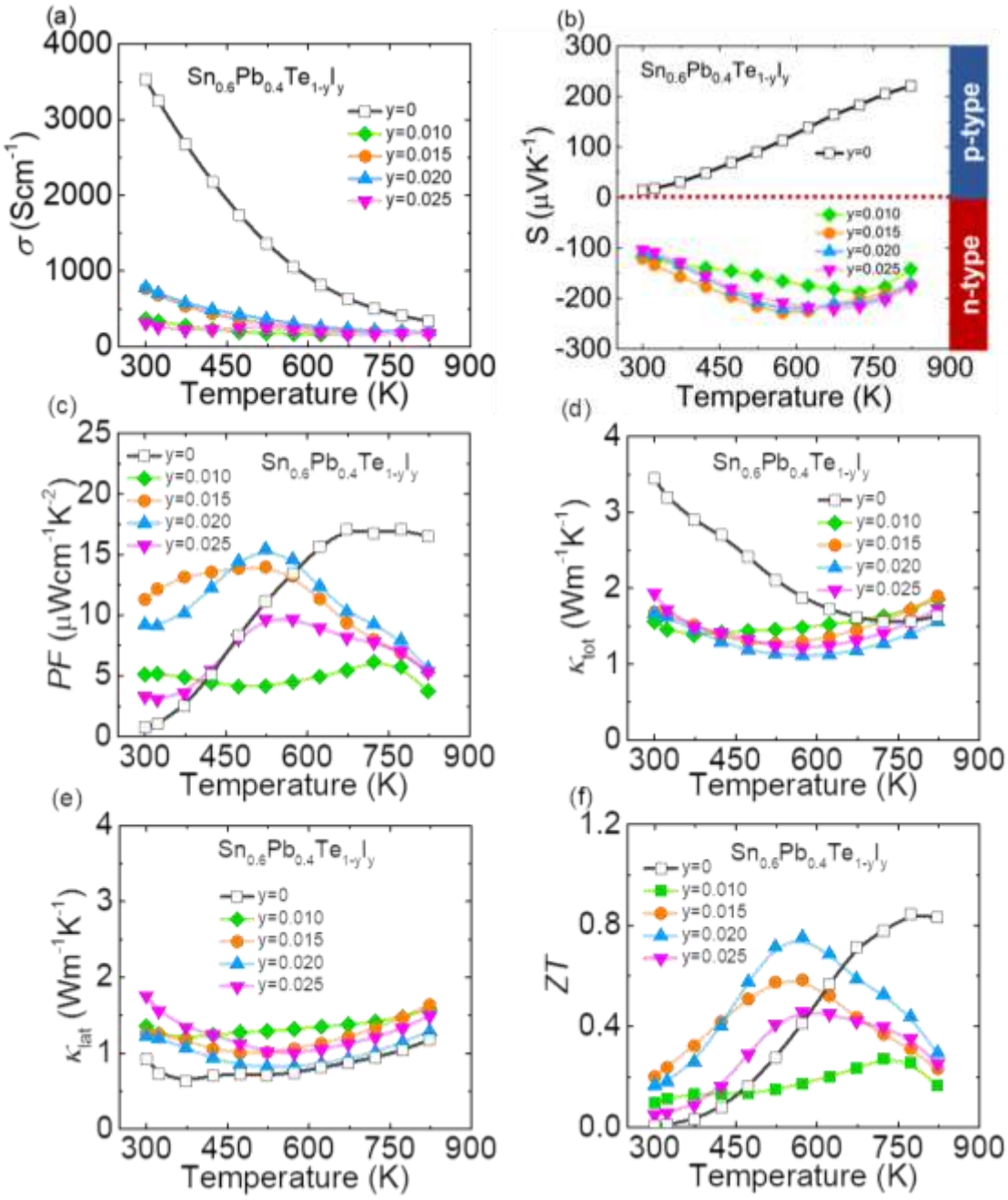

Figure S5. Thermoelectric transport properties as a function of temperature for $Sn_{0.6}Pb_{0.4}Te_{1-y}I_y$ (y = 0-0.025): (a) electrical conductivity; (b) Seebeck coefficient; (c) power factor; (d) total thermal conductivity; (e) lattice thermal conductivity; (f) *ZT* value.

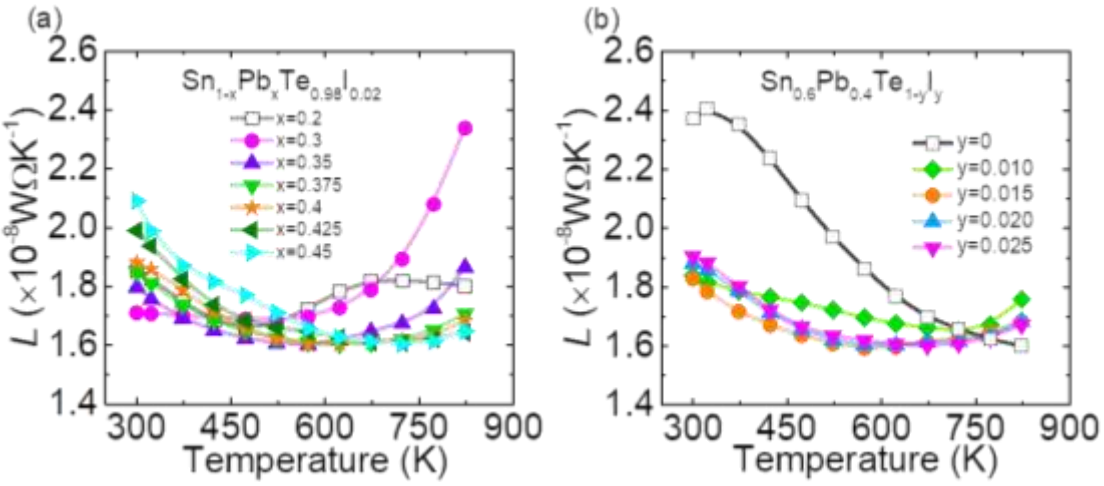

Figure S6. Lorenz numbers as a function of temperature for (a) $Sn_{1-x}Pb_xTe_{0.98}I_{0.02}$ (x = 0.2-0.45) and (b) $Sn_{0.6}Pb_{0.4}Te_{1-y}I_y$ (y = 0-0.025).

Table S1. Experimental and theoretical sample density and the relative ratio for SnTe-based samples.

Samples	Experimental density (gcm^{-3})	Theoretical density (gcm^{-3})	Relative ratio (%)
$Sn_{0.6}Pb_{0.4}Te$	7.072	7.191	98.34
$Sn_{0.6}Pb_{0.4}Te_{0.99}I_{0.01}$	7.027	7.180	97.87
$Sn_{0.6}Pb_{0.4}Te_{0.985}I_{0.015}$	7.019	7.186	97.67
$Sn_{0.6}Pb_{0.4}Te_{0.98}I_{0.02}$	6.969	7.176	97.13
$Sn_{0.6}Pb_{0.4}Te_{0.975}I_{0.025}$	6.979	7.180	97.20
$Sn_{0.8}Pb_{0.2}Te_{0.98}I_{0.02}$	6.643	6.819	97.42
$Sn_{0.7}Pb_{0.3}Te_{0.98}I_{0.02}$	6.851	6.993	97.97
$Sn_{0.65}Pb_{0.35}Te_{0.98}I_{0.02}$	6.901	7.090	97.34
$Sn_{0.625}Pb_{0.375}Te_{0.98}I_{0.02}$	6.940	7.139	97.21
$Sn_{0.575}Pb_{0.425}Te_{0.98}I_{0.02}$	7.074	7.215	98.05
$Sn_{0.55}Pb_{0.45}Te_{0.98}I_{0.02}$	7.146	7.269	98.31

The experimental sample density ρ_{exp} was determined by using the dimensions and mass of the samples, and the theoretical density ρ_{the} of the samples were calculated using:

$$\rho_{the} = \frac{\bar{M}}{\Omega} \tag{S25}$$

where $\bar{M}$ represents the average atom mass and Ω is the average atom volume.

Table S2. The experimentally measured lattice thermal conductivity (κ_{lat}) and sound velocity (v_l, v_s, v_a) of the samples at 300 K. The elastic properties (E, G, and υ_p), the Grüneisen parameter (γ) and the phonon mean free path (l) calculated using the sound velocities.

Samples	κ_{lat} ($Wm^{-1}K^{-1}$)	v_l ($m\ s^{-1}$)	v_s ($m\ s^{-1}$)	v_a ($m\ s^{-1}$)	E (GPa)	G (GPa)	υ_p	γ	l (nm)	θ_D (K)
$Sn_{0.6}Pb_{0.4}Te$	0.92	3244	1835	2041	60.2	23.8	0.26	1.57	1.10	190
$Sn_{0.6}Pb_{0.4}Te_{0.99}I_{0.01}$	1.35	3266	1840	2047	60.4	23.8	0.27	1.59	1.63	191
$Sn_{0.6}Pb_{0.4}Te_{0.985}I_{0.015}$	1.26	3263	1874	2081	61.8	24.6	0.25	1.52	1.49	194
$Sn_{0.6}Pb_{0.4}Te_{0.98}I_{0.02}$	1.22	3258	1844	2051	59.9	23.7	0.26	1.57	1.48	191
$Sn_{0.6}Pb_{0.4}Te_{0.975}I_{0.025}$	1.76	3268	1820	2027	59.0	23.1	0.28	1.63	2.15	189
$Sn_{0.8}Pb_{0.2}Te_{0.98}I_{0.02}$	1.66	3400	1918	2133	61.9	24.4	0.27	1.58	1.90	200
$Sn_{0.7}Pb_{0.3}Te_{0.98}I_{0.02}$	1.34	3469	1872	2090	62.2	24.0	0.29	1.74	1.57	195
$Sn_{0.65}Pb_{0.35}Te_{0.98}I_{0.02}$	1.45	3320	1863	2073	60.9	24.0	0.27	1.60	1.73	194
$Sn_{0.625}Pb_{0.375}Te_{0.98}I_{0.02}$	1.55	3301	1839	2048	59.8	23.5	0.28	1.63	1.87	191
$Sn_{0.575}Pb_{0.425}Te_{0.98}I_{0.02}$	1.63	3251	1829	2035	60.0	23.7	0.27	1.59	1.97	189
$Sn_{0.55}Pb_{0.45}Te_{0.98}I_{0.02}$	1.64	3214	1779	1982	57.8	22.6	0.28	1.65	2.03	185

κ_{lat}, v_l, v_s, v_a, E, G, υ_p, γ, l, θ_D are the Lattice thermal conductivity, Longitudinal sound velocity, Shear sound velocity, Average sound velocity, Young's modulus, Shear modulus, Poisson ratio, Grüneisen parameter, Phonon mean free path, and Debye temperature, respectively.

REFERENCES

1. Barthel, J., Dr. Probe: A software for high-resolution STEM image simulation. *Ultramicroscopy* **2018,** *193*, 1-11.
2. Xiao, Y.; Chang, C.; Pei, Y.; Wu, D.; Peng, K.; Zhou, X.; Gong, S.; He, J.; Zhang, Y.; Zeng, Z.; Zhao, L.-D., Origin of low thermal conductivity in SnSe. *Physical Review B* **2016,** *94* (12), 125203.
3. Wu, D.; Zhao, L.-D.; Tong, X.; Li, W.; Wu, L.; Tan, Q.; Pei, Y.; Huang, L.; Li, J.; Zhu, Y., Superior thermoelectric performance in PbTe–PbS pseudo-binary: extremely low thermal conductivity and modulated carrier concentration. *Energy and Environmental Science* **2015,** *8* (7), 2056-2068.
4. Qu, W.-W.; Zhang, X.-X.; Yuan, B.-F.; Zhao, L.-D., Homologous layered $InFeO_3(ZnO)_m$: new promising abradable seal coating materials. *Rare Metals* **2018,** *37* (2), 79-94.
5. Qin, B.; Wang, D.; He, W.; Zhang, Y.; Wu, H.; Pennycook, S. J.; Zhao, L.-D., Realizing high thermoelectric performance in p-type SnSe through crystal structure modification. *Journal of the American Chemical Society* **2019,** *141* (2), 1141-1149.
6. May, A. F.; Toberer, E. S.; Saramat, A.; Snyder, G. J., Characterization and analysis of thermoelectric transport in *n*-type $Ba_8Ga_{16-x}Ge_{30+x}$. *Physical Review B* **2009,** *80* (12), 125205.
7. Zhou, Y.; Wu, H.; Pei, Y.; Chang, C.; Xiao, Y.; Zhang, X.; Gong, S.; He, J.; Zhao, L.-D., Strategy to optimize the overall thermoelectric properties of SnTe via compositing with its property-counter $CuInTe_2$. *Acta Materialia* **2017,** *125*, 542-549.
8. Kresse, G.; Joubert, D. P., From ultrasoft pseudopotentials to the projector augmented-wave method. *Physical Review B* **1999,** *59* (3), 1758-1775.
9. Kresse, G.; Furthmuller, J., Efficient iterative schemes for ab initio total-energy calculations using a plane-wave basis set. *Physical Review B* **1996,** *54* (16), 11169-11186.
10. Perdew, J. P.; Burke, K.; Ernzerhof, M., Generalized gradient approximation made simple. *Physical review letters* **1996,** *77* (18), 3865-3868.
11. Medeiros, P. V. C.; Stafström, S.; Björk, J., Effects of extrinsic and intrinsic perturbations on the electronic structure of graphene: Retaining an effective primitive cell band structure by band unfolding. *Physical Review B* **2014,** *89* (4), 041407.
12. Medeiros, P. V. C.; Tsirkin, S. S.; Stafström, S.; Björk, J., Unfolding spinor wave functions and expectation values of general operators: Introducing the unfolding-density operator. *Physical Review B* **2015,** *91* (4), 041116.
13. Toberer, E. S.; Rauwel, P.; Gariel, S.; Taftø, J.; Jeffrey Snyder, G., Composition and the thermoelectric performance of β-Zn_4Sb_3. *Journal of Materials Chemistry* **2010,** *20* (44), 9877-9885.
14. Bardeen, J.; Shockley, W., Deformation potentials and mobilities in non-polar crystals. *Physical Review* **1950,** *80* (1), 72-80.
15. Callaway, J.; von Baeyer, H. C., Effect of point imperfections on lattice thermal conductivity. *Physical Review* **1960,** *120* (4), 1149-1154.